Mechanisms of Ion Irradiation Induced Ordering in Amorphous TiO₂ Nanotubes: Effects of Ion Mass and Energy

Tristan Olsen, Wei-Ying Chen, Miu Lun Lau, Cyrus Koroni, Chao Yang, Md Ali Muntaha, Sarah Pooley, Zhongxia Shang, Dewen Hou, Ling Wang, Min Long, Janelle P. Wharry, Hui Xiong

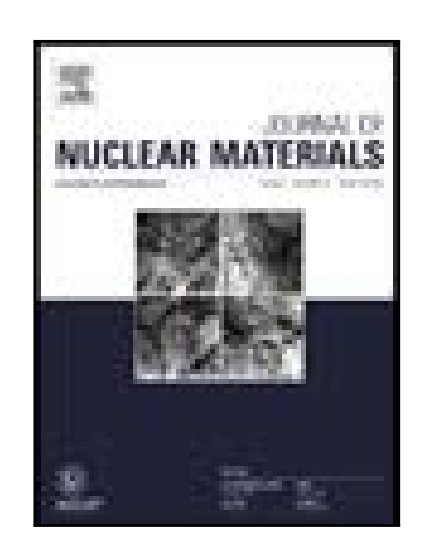
PII: \$0022-3115(24)00216-2

DOI: https://doi.org/10.1016/j.jnucmat.2024.155114

Reference: NUMA 155114

To appear in: Journal of Nuclear Materials

Received date: 4 January 2024 Revised date: 18 April 2024 Accepted date: 19 April 2024



Please cite this article as: Tristan Olsen, Wei-Ying Chen, Miu Lun Lau, Cyrus Koroni, Chao Yang, Md Ali Muntaha, Sarah Pooley, Zhongxia Shang, Dewen Hou, Ling Wang, Min Long, Janelle P. Wharry, Hui Xiong, Mechanisms of Ion Irradiation Induced Ordering in Amorphous TiO₂ Nanotubes: Effects of Ion Mass and Energy, *Journal of Nuclear Materials* (2024), doi: https://doi.org/10.1016/j.jnucmat.2024.155114

This is a PDF file of an article that has undergone enhancements after acceptance, such as the addition of a cover page and metadata, and formatting for readability, but it is not yet the definitive version of record. This version will undergo additional copyediting, typesetting and review before it is published in its final form, but we are providing this version to give early visibility of the article. Please note that, during the production process, errors may be discovered which could affect the content, and all legal disclaimers that apply to the journal pertain.

© 2024 Published by Elsevier B.V.

Mechanisms of Ion Irradiation Induced Ordering in Amorphous TiO₂ Nanotubes: Effects of Ion Mass and Energy

Tristan Olsen^a, Wei-Ying Chen^b, Miu Lun Lau^c, Cyrus Koroni^a, Chao Yang^d, Md Ali Muntaha^d, Sarah Pooley^a, Zhongxia Shang^d, Dewen Hou^a, Ling Wang^e, Min Long^b, Janelle P. Wharry*^d, Hui Xiong*^a

- a Micron School of Materials Science & Engineering, Boise State University, 1910 University Drive, Boise ID 83725. E-mail: clairexiona@u.boisestate.edu.
- ^{b.} Argonne National Laboratory, 9700 S Cass Avenue, Lemont IL 60439.
- ^{c.} Department of Computer Science, Boise State University, 1910 University Drive, Boise ID 83725.
- ^{d.} School of Materials Engineering, Purdue University, 205 Gates Road, West Lafayette IN 47906 E-mail: <u>iwharry@purdue.edu</u>.
- e. SLAC National Accelerator Laboratory, 2575 Sand Hill Rd, Menlo Park, CA 94025

Amorphous TiO₂ nanotubes were irradiated *in-situ* in a transmission electron microscope (TEM) with Kr* ions at energies of 46 keV, 150 keV, and 1 MeV and with 46 keV Xe* ions, to investigate the structural and morphological evolution of the nanotubes under irradiation. At all irradiation conditions, amorphous TiO₂ nanotubes exhibited significant morphological instability, and tended to undergo volumetric swelling with increasing ion counts, often until collapse of the original nanotube structure. Molecular dynam. (MD) simulations confirmed that irradiation-induced defects can explain the observed swelling. Structurally, nanotubes remain amo, hous following all Kr* irradiation conditions, but irradiation with 46 keV Xe* leads to the formation of anatase nanocrystallites. Poor antly, through systematically varying ion energy and ion species, we try to elucidate the influence of nuclear and electronic stop ing pover on ion irradiation induced changes. By contextualizing these results within the existing literature, we propose that the observed and in TiO₂ nanotube morphology and structure could be due to a competition between two mechanisms: (1) disorder-induced line, and, (2) irradiation-induced amorphous-to-crystalline transformation.

1. Introduction

Titanium oxide materials, especially TiO₂, has attracte it considerable attention in the nuclear industry and beyond due to their unique properties. For example, its high reference index, high dielectric constant, chemical stability, and photocatalytic properties have made TiO₂ and tree rely attractive material for applications such as radiation detectors, sensors and instrumentation for both in-pile and out-of-pile applications, thin film coatings for dielectric mirrors, nuclear waste and actinide separation, and ti-ceramic candidate materials for future tritium breeding reactors. ¹⁻⁸ Nanostructured materials for nuclear application, and the particularly attractive, because their high surface area to volume ratio of nanostructured materials tend of an acceptance to irradiation induced damage. ⁹ Intrinsically, amorphous ceramic materials are assection, dered to have high resistance to irradiation induced damage, but they have received less attention than crystal ineceramics, and the underlying mechanisms behind their radiation resistance is less well understood. ¹⁰ Due to their exposure to extreme environments associated with nuclear reactors and nuclear waste, it is of both scientific and technologic interest to understand the effects of irradiation damage on ceramic materials like TiO₂ nanotubes.

In our previous w rk, we have shown that proton irradiation of amorphous and anatase TiO₂ NTs can be utilized to improve their electro hemical performance either by transforming amorphous material into disordered polycrystalline structures, or by creating irradiation induced defects without significantly changing the original NT morphology and crystal structure. In another study, we have shown that irradiation of amorphous TiO₂ NTs with Au ions leads to a transformation from amorphous to anatase TiO₂, and in cases where the transformation is only partially complete, internal stress due to the densification of the amorphous-to-crystalline transformation (a-to-c) causes bending and curling of the NT. In irradiation-induced damage in materials is generally understood to be caused by the transfer of energy from energetic particles to the target material - leading to ionization and displacement of atoms. Energy transfer from the incident particle to the target material occurs through either nuclear and/or electronic stopping. This energy transfer mode is ultimately responsible for the variety of irradiation-induced defects and structural and morphology changes that occur in irradiated materials. While the effects of ion irradiation on crystalline ceramic materials - such as TiO₂ - has been moderately well studied and shares similarities with the more thoroughly understood irradiation effects in metallic crystals, the effects of irradiation on amorphous ceramics are not well understood. Moreover, there is a significant gap in our understanding of the underlying mechanisms for irradiation-induced structural and

morphological changes in amorphous ceramics, such as the a-to-c transformation; current knowledge is based on conjecture from only a few studies. 10,15

In the present study, we explore the effects of Kr⁺ and Xe⁺ on the structure and morphology at various energies so that we can elucidate how ion energy, and nuclear and electronic stopping power influence ion irradiation induced changes. *in-situ* ion irradiation using Kr and Xe of individual TiO₂ nanotubes is novel in the existing literature, and utilizing noble gas ion species in this way also has the advantage of eliminating possible doping or chemical bonding effects. We observed the structural and morphological changes of amorphous TiO₂ NTs irradiated with Kr⁺ and Xe⁺ ions at systematically varied energies, *in-situ* within a transmission electron microscope (TEM). To help elucidate the observed morphological changes in the irradiated TiO₂ NTs, molecular dynamics (MD) and Stopping and Range of Ions in Matter (SRIM) simulations are performed. Results point toward two competing mechanisms that govern the irradiation-induced morphological evolution of the amorphous NTs. These findings present a significant opportunity for harnessing irradiation to tailor the structure, phase composition, and morphology of TiO₂ NTs to intentionally design desired material properties and functionalities.

2. Methods

2.1 Material Synthesis, Irradiation, & Characterization

The TiO₂ nanotubes used in this study were synthesized via electrochemical a odiz tion, and details of this process have been previously published in other works. ^{11,12} To summarize, titanium for (32 μm, 99.8%, Alfa Aesar) was cleaned by sonication in three steps using acetone, isopropanol, and nanc sure ce-ionized (DI) water for 5 minutes. Anodization was carried out in a two-electrode cell against a platinum ness. Sunter electrode in a 0.27 M solution of ammonium fluoride in 95% formamide/water. Samples were then and dized for 20 minutes at a constant voltage of 20 V. The anodized samples were then rinsed in water and sonicated for 1) seconds in nanopure DI water and allowed to dry in air. The as-prepared samples were confirmed to be amorphous as shown by x-ray diffraction (XRD) measurement, as all diffraction peaks in the pattern were part iffied as belonging to the Ti substate and not the TiO₂ layer (Fig. 1).

Samples for the *in-situ* ion irradiation experiments were prepared by scraping the as-prepared TiO₂ nanotubes off of the Ti foil substrate, and placing them onto care in film TEM grids. The *in-situ* ion irradiation was conducted at the Intermediate Voltage Electron Microscopy-Tandem (IVEM-Tandem) facility located at Argonne National Laboratory (ANL). Four ion irradiations were carried out at room temperature using Kr+ ions at 46 keV, 150 keV, and 1 MeV and Xe+ ions at 46 keV. The beam flux was 6.55 × 10¹¹ ions/cm²/s, to a total fluence of 1.9 x 10¹⁵ – 4.6 x 10¹⁵ ions/cm² depending on the irradiation combination. Note that during the experiments, the dose was represented by the unit of "counts", where there is a fluence of 1.0 x 10¹⁰ ions/cm² per count; the total dose for 46 keV Kr, 150 keV Kr, and 46 keV Xe irradiations was there are 30,000 counts. For 1 MeV Kr, the fluence was 6.25 x 10⁹ ions/cm² per count. A summary of the irradiation conditions used for each experiment is shown in Table 1. TEM video and images were collected throughout the cope iment, at intervals of 50,000-100,000 counts. TEM was conducted using an accelerating voltage of 200 kV. S ibsection that intervals of 50,000-100,000 counts. TEM was conducted using an accelerating voltage of 200 kV. S ibsection analysis of nanotube length, outer diameter, inner diameter, wall thickness, and volume were made of each parameter to ensure reliability, and uncertainty in the measurements was calculated as a result.

Table 1. Summary of irradiation conditions and resulting changes in the current study of amorphous TiO2 nanotubes.

Ion species	Energy (keV)	Fluence (ions/cm ²)	Fluence per count (ions/cm²/count)	Total counts
Xe ⁺	46	3.9 x 10 ¹⁵	1.3 x 10 ¹⁰	300k
$\mathrm{Kr}^{\scriptscriptstyle +}$	46	3.9 x 10 ¹⁵	1.3×10^{10}	300k

Kr ⁺	150	4.6×10^{15}	1.3×10^{10}	350k
Kr^{2+}	1000	1.9×10^{15}	6.25 x 10 ⁹	300k

Vacancy and ion range plots for the aforementioned irradiation conditions were calculated using the 2013 version of Stopping Range of Ions in Matter (SRIM). Damage calculations were performed using the "Detailed Calculations with Full Damage Cascades" mode. Because SRIM cannot simulate nanostructured materials, the TiO₂ nanotube wall thickness was approximated as a homogeneous slab of amorphous TiO₂ with a density of 2.43 g/cm³ and a maximum thickness of 1200 nm. The density of amorphous TiO₂ was determined using a molecular dynamics (MD) method detailed in a prior publication. He displacement energies for titanium and oxygen were set to the default values of 25 and 28 eV, respectively, and simulations were run to a minimum of 250,000 ion Life ories to ensure statistically significant results. Nuclear and electronic stopping powers in the simulated amorphous TiO₂ were calculated using the "Ion Stopping and Range Tables" in SRIM.

Following irradiation, the 46 keV Kr⁺ and Xe⁺ irradiated nanotubes were more closely examined for phase and structural transformation using aberration-corrected high-resolution T' M (LTC-TEM) in a Thermo Fisher Scientific Themis Z S/TEM at the Birck Nanotechnology Center at Purdue J in ers ty. Atomic resolution HR-TEM was conducted at 300 kV accelerating volage, and the corresponding 1 st Fi urier transformations (FFT) was used to gauge the degree of disorder.

2.2 Molecular Dynamics Simulations

MD simulations of energetic Kr and Xe ions inc act to amorphous TiO₂ nanotubes were carried out using Large-scale Atomic/Molecular Passively Parallel Simulation (LAMMPS)¹⁸ with a hybrid interatomic potential of Reaxff and Ziegler-Biersack-Littmark (ZBL).^{19,20} The ZBL potential was utilized to model the nuclear repulsion during high-energy collisions between the incident irradiating ions and the target atoms. The ZBL potential was employed between 2.5 and 3.5 Å, while Rexaff is used to produce the interatomic potential at all other interatomic distances. The initial geometry was obtained from materials projectory, and visualized using Visualization for Electronic and Structural Analysis (VESTA).²⁷ Generation and produce a proposed using two methods: (1) LAMMPS and (2) VESTA to verify the resultant nanotube geometry was amorphous.

The structure was first related in the isothermal isobaric (NPT) ensemble at 300 K and 1 atm for 20 ps. Subsequently, to simulate the irrad ation process, 46, 150, and 1000 keV Kr ions were injected toward the bulk material at regular intervals of 1000 kmc ters with a total period of 40 ps, corresponding to a dose of 9.4 x 10¹⁵ ions/cm². For Xe, 46 keV ions were injected unler the same conditions. Due to the significant thermal energy introduced to the system during the irradiation and ato....c displacement processes, a 10 Å thermostatic boundary layer was set around the domain to emulate the phonon-assisted energy dissipation. After the conclusion of irradiation, the structure was allowed to relax under NPT ensemble conditions for an additional 20 ps to simulate the irradiation recovery within the system.

The volume evolution as well as the vacancy and interstitial defect populations were monitored after irradiation. The volume was monitored only during the post-irradiation relaxation stage. The point defect analysis was monitored using the Wigner-Seitz (WS) cell method²¹, which enabled quantification of the number of vacancies, interstitials, and antistites produced from the irradiation. OVITO was used to create the analysis pipeline with a Python script. ²² For the vacancy and interstitial pipeline, the cell size was compared to the unirradiated cell, and sites were identified as containing a vacancy (lack of any atoms) or an interstitial (more than one atom on a site). The MD WS cells before and after ion injection and diffusion are shown in Figures 2 and 3.

3. Results

3.1 Morphological Evolution of Nanotubes

Nanotubes tend to have a heterogeneous response to irradiation. For example, irradiation with 46 keV Kr⁺ ions appear to affect some nanotubes more than others under in-situ ion irradiation (arrows, Fig. 4). For the purpose of this study, we highlight nanotubes that show the most significant morphological changes as a result of ion irradiation at all conditions. Additionally, images for 1 MeV irradiation were included in Figure 5 so that we would have an example of irradiation effect at high ion energy, and high electronic-to-nuclear stopping power. However, our results and discussion will mainly focus on the irradiation conditions at lower energies, due to limitations that prevented us from tracking a single tube irradiated to 1 MeV consistently throughout the experiment. For the specimens highlighted in this study, all four irradiation conditions result in significant morphological changes to the TiO2 nanotubes (Fig. 5) with greater morphological instability with increasing ion counts. Specifically, the thickness of the tube walls increases while the tube length and inner diameter decreases as a function of ion count; this behavior is tracked throughout the irradiations for selected tubes oriented with their long axis perpendicular to the ion beam direction, i.e., "side-view" (Fig. 5a-r, and Fig. 6a-d). The wall thickness evolution can also be seen for the 150 keV Kr⁺ irradiation, in which one of the tracked tubes is oriented with its long axis parallel to the beam direction (Fig. 7). The morphological evolution appears to be similar regardless of the tube orientation with respect to the ion beam direction. Fe tubes irradiated with 1 MeV Kr²⁺, the nanotube morphology appears to be significantly altered (Fig. 5k-n) comparation, wer energy Kr+ irradiated specimens (Fig. 5b and 5g). Overall, nanotube morphological evolution is mo. proj ounced at lowest and highest ion energies. i.e., 46 and 1 MeV for Kr⁺, and 46 keV for Xe⁺.

Nanotube morphology measurements are taken of the 46 keV Kr⁺, 15c keV Kr⁺, and 46 keV Xe⁺ ion irradiated samples, specifically focusing on nanotube length, outer diameter, inner di me, r, and the wall thickness evolution as a function of ion fluence, Fig. 6. Nanotube length decreases rapidly with fluence Fig. 6a). For 46 keV Kr+, the length appears to reach a 'steady state' in which tube length ceases to decrease significantly after about 100k counts, while Kr⁺ at 150 keV is still decreasing up to 350k counts. Although a reference unirradiated (i.e., 0 counts) image is not available for 46 keV Xe^+ , the tube length appears to be at steady-state $y < 00^\circ$, counts. The outer diameter of the nanotube walls remains nearly constant, or grows slightly, acro's a irr diation conditions (Fig. 6b). Meanwhile, the inner diameter reduces rapidly with dose (Fig. 6c), resulting nov rall nanotube wall thickness increases (Fig. 6d). Examining the percent change of nanotube wall thickness at fixe. dose intervals - such as 0-50k, 50-100k, and 100-200k counts reveals that wall thickness change is higher at ~100% for Xe over 0-50k counts, while changes over 50-100k and 100-200k are comparatively lower at ~13-2' Th. other two conditions follow a similar pattern, with the exception of Kr at 46 keV having its second highest volume change over 100-200k counts.

Nanotube volume estimates ba ea 'n TEM dimensions are made using the equation:

$$V = \pi h(R - r)^2$$

1 where h is the nanotube length R is the radius of outer diameter, and r is the radius of the inner diameter. The increase in nanotube volume is calc. lated over 50-200k counts and confirms that the irradiation indeed causes volumetric swelling (Fig. 8\ In Fig. c), the largest observable change in nanotube volume occurs for Xe at 46 keV between 50-100k counts, with ne. ...nt increase of 21.6±0.8%. Kr at 46 and 150 keV comparatively experience much smaller percent changes of -0 7±0.7 and 3.2±0.9%, respectively. This seems to highlight a trend in which Xe ion implantation at 46 keV initially causes a greater change in wall thickness and tube volume than Kr at the same energy, but Kr experiences a larger percent change at higher ion counts. At all the ion counts highlighted in Fig. 6e-f, Kr at 46 keV experience significantly larger changes in wall thickness and volume than Kr at 150 keV. The total percent change for all three conditions highlighted in Fig. 6f between 50-200k for 46 keV Kr, 150 keV Kr, and 46 keV Xe counts is $34.3\pm0.1\%$, $8.2\pm0.1\%$, and $35.5\pm0.1\%$, respectively.

The measured wall thickness of the unirradiated nanotubes falls in the range of 10-15 nm (Fig. 6d), but the peak vacancy concentrations are predicted to occur at a depth of about 24 nm for 46 keV Kr⁺ and 18 nm for Xe⁺ (Fig. 9a,b). Assuming irradiating particles are incident normal to the nanotube wall, more Xe+ ions than Kr+ ions interact with the tube walls, and thus Xe⁺ ions transfer more energy and create more extensive damage and disorder. The greater efficacy of Xe+ ions at creating damage is also evidenced by reaching steady-state wall thickness (and possibly also length) at a lower fluence than does the same energy of Kr⁺ ions (Fig. 6a,e). Ion energy alters the electronic-to-nuclear stopping power ratio (Fig. 9c,d), with the lowest ratio occurring at ion energies of 46 keV, and increasing to nearly unity at a Kr⁺

energy 1 MeV. This stopping power ratio evolution is evidenced by the more pronounced changes in nanotube morphology for the 46 keV irradiations than for the 150 keV Kr⁺ irradiation (Fig. 5), suggesting that nuclear stopping (more so than electronic stopping) may be responsible for the observed nanotube morphological changes.

3.2 Structural Evolution

Selected area electron diffraction (SAED) patterns collected on the IVEM-Tandem during the irradiation experiments appear to suggest that the 46 keV Kr⁺ and Xe⁺ irradiated nanotubes remain amorphous after irradiation (Fig. 10). However, due to the resolution limits of SAED, high resolution TEM (HR-TEM) characterization with fast Fourier transformations (FFT) are needed to confirm the atomic structures. Post-irradiation HR-TEM atomic resolution imaging indeed confirms that the 46 keV Kr⁺ ion irradiated nanotubes remain amorphous following irradiation (Fig. 11a-d). Three different nanotubes located adjacent to one another, are characterized, as indicated in Fig. 11a. All three tubes remain straight and maintain their structural integrity throughout irradiation, and atomic resolution imaging suggests a disordered atomic arrangement in the nanotubes. FFT diffractograms of the HR-TEM images consistently confirm the amorphous nature of the nanotubes.

By contrast, HR-TEM with FFT of the 46 keV Xe⁺ ion irradiated nanotubes exhi. it irradiation-induced nanocrystallization (Fig. 11e-h). Although these nanotubes again remain straight and maintain their structural integrity, nanocrystallites form throughout the amorphous matrix. While the rutile polyr iorp, is more stable in bulk TiO₂, anatase phase is more thermodynamically stable in nanostructured materials due to the, high surface area-to-volume ratio and the predominance of surface effects.^{23,24} The anatase nanocrystallites ran e ~5.3 nm in diameter and appear to be distributed relatively homogeneously throughout the nanotube. Atomic results non HR-TEM shows defined crystalline planes within the nanocrystallites, and FFT diffractograms also show indications of discrete diffraction spots, providing confirmatory evidence of the irradiation-induced nanocrystallization.

3.3 Molecular Dynamics

MD simulations show that O vacancies form by ~ 50 pc at other population increases rapidly before approaching steady-state by ~ 125 ps, (Fig. 12a). The O intersolved is form ~ 25 ps after vacancies, due to the nature of a Frenkel pair requiring a displaced atom to first create a vacancy before it becomes an interstitial. The O interstitial population remains slightly lower than the O vacancy population, but also converges to steady-state by ~ 125 ps. The Ti vacancies follow a similar trajectory, forming by ~ 5 ps and reaching steady-state by ~ 100 ps (Fig. 12b). However, Ti interstitials form significantly slower, starting at ~ 90 ps, and never reaching steady-state during the ~ 200 ps simulation. The difference in O and Ti defect species it does not eated by Xe⁺ than by Kr⁺, which is consistent with the higher nuclear stopping power of Xe⁺ than Kr⁺.

Fig. 12c shows that increasin, in diation fluence also corresponds to an increase in volume for a simulated amorphous Wigner-Seitz cell. In keeping vith the higher defect population from Xe+, the volume change over time is also predicted to be greater for Xe+ than for Kr+ irradiation, which also supports experimental results showing nanotube volume increase as a function of ion counts is overall higher for 46 keV Xe+ compared to 46 keV Kr+ (Fig. 6f, and Fig. 8). This suggests that although greater nuclear stopping may not necessarily cause greater total volumetric swelling of nanotubes, it result in more rapid point defect generation which can induce more rapid dimensional changes and consequently faster convergence toward a steady-state irradiated tube volume.

4. Discussion

The extent of irradiation-induced swelling of the nanotubes can be explained by the position (depth) of the damage peak, which is controlled by the irradiating ion energy and species. Assuming the most conservative condition in which the irradiating particles are laterally - rather than axially - incident on the nanotube walls, only the 46 keV Kr^+ and Xe^+ irradiation conditions will fully deposit their energy within the nanotubes. That is, the SRIM predicted damage peaks are located within the nanotube wall thickness. Such a configuration can explain the more extensive morphological changes in the 46 keV irradiations as compared to the 150 keV. In addition, the higher mass of Xe^+ compared to Kr^+ will generate a larger damage cascade 15,25 , which can explain the greater initial wall thickness increases over 0-50k counts due to $46 \text{ keV } Xe^+$ than from $46 \text{ keV } Kr^+$.

To understand these observed morphological changes, the present results are considered in the context of the archival literature. Often, irradiation of amorphous materials with charged particle (i.e., ion or electron) beams results in the formation of nanocrystallites through an amorphous-to-crystalline (a-to-c) phase transformation. ^{10,13,26,27} In a previous work on similar amorphous TiO₂ nanotubes as studied herein, Au⁻ ion irradiation induces the a-to-c transformation which leads to tube bending and curling; ¹⁴ this and the current study are summarized in Table 2. This table suggests that two major potentially competing phenomena manifest as morphological evolution of the nanotubes: (1) swelling and (2) a-to-c transformation. The extent to which each of these phenomena occur can be explained by the electronic-to-nuclear (e-to-n) stopping power ratios. Recall that nuclear stopping describes elastic collisions involving primary knock-on displacement damage leading to Frenkel pair defect production within a cascade, whereas electronic stopping describes a wide variety of inelastic collisions producing variable excitation of valence electrons that can generate atomic displacements along the incident ion path and not necessarily in a cascade. ²⁸

4.1 Irradiation-Induced a-to-c Transformation

$$\rho C_p \frac{\partial T}{\partial t} = \nabla \cdot k \nabla T + Q$$
 2

Here, ρ is the density of the target material, C_p is the specific heat of the arget material, k is thermal conductivity, and Q is the heat generation rate. This heat generation rate is a function of the thermal spike descriptors:

$$Q = \frac{q_s}{V_t}$$

where q_s is the thermal spike energy, V_s is thermal spike volume, and t_s is the thermal spike duration. The thermal spike, however, must be considered within the context of phase transformation mechanisms.

Table 2. Summary of irradiation conditions and resulting many and prior and current studies of amorphous TiO₂ nanotubes.

Ion species	Energy (keV)	Fluence (ions/cm ²)	Flux (ions/cm ² /s)	lon mass (/mol)	Electronic-to- nuclear stopping ratio	a-to-c Transformation	Volumetric swelling	Ref.
Xe ⁺	46	3.9 x 10 ¹⁵	6.25 (1)	131.29	0.080	Partial	Most swelling	This study
Au ⁻	46	2.3 x 10-	7.7 x 10 ¹¹	196.97	0.104	Complete	No swelling	Ref ¹⁴
Kr^+	46	3.9 × 10 ¹⁵	6.25 x 10 ¹¹	83.80	0.115	No	Most swelling	This study
Kr^+	150	4.6 x 10 ¹⁵	6.25 x 10 ¹¹	83.80	0.212	No	Some swelling	This study
Kr^{2+}	1000	1.9 x 10 ¹⁵	6.25 x 10 ¹¹	83.80	0.789	No	Some swelling	This study

The mechanism for irradiation-induced a-to-c transformation is not well understood. ¹⁰ Qin et al. provides an athermal transformation hypothesis, ³⁰ owing to the fact that the majority of irradiation-induced a-to-c transformations reported in the literature occur at ambient irradiation temperatures well below the crystallization temperature. ^{10,27,30} Qin's hypothesis is based upon the assumption that the initial amorphous phase is a high energy metastable state, while the crystalline structure is a lower energy state that can be achieved when energy is injected into the system (i.e., by the irradiating particles). This energy injection affects the system in two ways: first by forming point defects stored within the original amorphous phase (ΔE_{sto}), and second by stimulating the amorphous phase. The stimulation relaxes by

undergoing atomic rearrangements, attempting to return to a lower-energy state. During these rearrangements, the system could return to the original amorphous phase containing the irradiation-induced stored point defects. However, the system may be able to release even more energy by rearranging into a crystalline state with energy ΔE_{rea} lower than the original amorphous state. This rearrangement into crystallization will proceed if:

$$\Delta E_{rea} > \Delta E_{sto}$$

In other words, the a-to-c transformation proceeds only when it is energetically favorable to crystallize rather than to maintain point defects in the amorphous state. The left-hand side of this inequality can be assumed to be constant, while the right-hand side will differ for each irradiation condition in Table 2.

To explain the phase transformations observed herein, let us consider two bounding cases of high and low electronic-to-nuclear stopping power ratios. In cases of high electronic-to-nuclear stopping power ratios, the irradiating particle transfers the majority of its energy to the target material through numerous electronic interactions along the ion track - often up to \sim 10 nm in diameter and \sim 100s nm or more in length. ³¹ Although defects are generated along the entire ion track, the thermal spike will consequently anneal many of these defects, driving down ΔE_{sto} . This makes the inequality in Eq. 4 easier to satisfy, thus favouring irradiation-induced a-to-c transformation. However, ion tracks are not observed herein due to the orders-of-magnitude lower e-to-n stopping power ratio than the M_2V -GeV energies used by Qin et al. ³¹. But as in the present study, irradiation induced a-to-c transformations have been c-bserved in many ceramic materials at ion energies much lower than 1 MeV. ¹⁰

The other bounding case, in conditions with low electronic-to-nuclear stopping power ratios, defects are generated in dense damage cascades, typically ~few nm in diameter assuming a spt eric. Lascade, rather than along ion tracks. MD simulations concur that defects nucleate and accumulate slightly r = rac jidly from Xe⁺ irradiation than Kr⁺ irradiation (Fig. 12). This would suggest that cascade damage is more extendive for lower electronic-to-nuclear stopping power ratios, which could increase ΔE_{sto} . But on the other hand, the thermal spike energy, q_s , is distributed over a smaller volume, V_s , than in a case of high electronic-to-nuclear stopping power ratio. Consequently, the heat generation rate Q (Eq. 3) is larger for lower electronic-to-nuclear stopping power ratio. Defect annealing occurs more readily, driving down ΔE_{sto} in a localized area, making irradiation-ind and a to-c transformation more favourable.

Although the range of e-to-n stopping power rat. s summarized in Table 2 is smaller than the extreme cases described in the two preceding paragraphs, trends c. be extracted which support observations that the Xe^+ and Au^- irradiations are more likely to satisfy the inequality and in duce the a-to-c transformation than Kr^+ irradiation. A similar phenomenon has been observed in into the trule materials, 32 in which "cascade-producing" (i.e., low electronic-to-nuclear stopping power ratio) irradiation, at inducing ordering of initially disordered Cu_3Au . More generally for the TiO_2 nanotube configuration, the h_1 h surface-area-to-volume ratio accelerates defect annihilation at surfaces, which inherently limits the energy h at c in be stored in point defects (ΔE_{sto}). This suggests that nanostructuring could make materials inherently more use ptible to irradiation-induced a-to-c transformation than bulk materials.

4.2 Defect-Driver Swalling

Retention of irradiat. n-induced defects in the amorphous phase (i.e., non-zero ΔE_{sto}) can drive swelling in tubes - or regions of tubes - i.ere rearrangement does not proceed. At a vacancy defect, localized decreases in electron bond density occur; the atom displaced from this vacant site then relocates to another site. This defect repositioning mechanism ultimately leads to volumetric expansion or swelling, similar to the "viscous flow" observed in nanomaterials such as Si nanopillars, in which irradiation-induced vacancies diffuse, leading to material redistribution. All Hence, irradiation conditions with less extensive thermal spike-induced annealing of defects - specifically cases of high electronic-to-nuclear stopping power ratios – will have higher ΔE_{sto} and thus greater tendency to swell. Both a-to-c transformation and swelling occur simultaneously during 46 keV Xe⁺ irradiation, likely because of the extremely low electronic-to-nuclear stopping power ratio. In this case, the cascade is so extensive that a considerable defect population remains in the material (i.e., high ΔE_{sto}), although the thermal spike can anneal enough defects to make a-to-c transformation somewhat favorable, resulting in partial crystallization.

After significant increases in nanotube wall thickness, the tube structure may collapse upon itself, causing the structure to relax into a morphology with lower surface area. Volume expansion has been reported in the literature as a primary mechanism for irradiation-induced morphological changes in nanostructured materials^{35,36}, but it is unknown whether

this expansion is a precursor to – or perhaps completely unrelated to – the widely-studied phenomenon of irradiation-induced void swelling in solids.^{37–40} Notably, no evidence of void formation is observed in the present study.

Irradiation-induced morphological evolution in amorphous TiO₂ nanotubes appears to be a competition between disordering and ordering; the relative amounts of nuclear to electronic energy losses can explain the tendencies toward disordering or ordering. However, other factors are likely also at work. In reported literature, electron irradiation - which has a nearly infinite electronic-to-nuclear stopping power ratio - has often been shown to induce a-to-c transformations in ceramic materials in a highly dose dependent function.¹⁰ Meanwhile ion irradiation-induced a-to-c transformations have also been suggested to be dependent on dose, dose rate, and irradiation time. ¹⁰ Future studies to deconvolute the role of dose (i.e., fluence) and dose rate are warranted.

5. Conclusions

Amorphous TiO₂ nanotubes are irradiated *in-situ* within a TEM using Kr⁺ ions at 46 keV, 150 keV, and 1 MeV, and using Xe⁺ ions at 46 keV. All irradiation conditions result in significant morphological changes to the nanotubes. The highest energy conditions destabilize nanotube structure, while the lowest energy conditions cause swelling in dimensions, wall thickness, and volume of the nanotubes. MD simulations attribute the volumetric swelling of the nanotubes to Ti and O point defects created during irradiation. A partial a-to-c transformation occurs only in the 46 keV Xe⁺ irradiation, which has a lower electronic-to-nuclear stopping ratio as compared to 46 keV Kr⁺. By considering these results in the context of the literature, we identify two competing mechanisms in the nanotube morphological evolution under irradiation, controlled by the electronic-to-nuclear stopping power ratio: (1) defect-driven swelling and (2) irradiation-induced a-to-c transformation.

Author contributions

H. Xiong and J. Wharry conceptualized the work. T. Olsen prepared the san ples and analysed all data. W.-Y. Chen conducted the *in-situ* TEM experiments. M. L. Lau conducted MD simulations, M. Muntaha and M. Long assisted with discussion of the MD simulations. C. Yang, Z. Shang, D. Hou conducted post motion tem and data analysis. S. Pooley assisted sample preparation and data analysis. L. Wang helped with the lactic ization. T. Olsen, J. Wharry, and H. Xiong wrote the manuscript and all authors participated in reviewing and revision of the manuscript.

Conflicts of interest

There are no conflicts to declare

Acknowledgements

This research was supported by the National Science Foundation awards DMR-1838604 and DMR-1838605. *In-situ* TEM experiments were supported by the US Department of Energy, Office of Nuclear Energy, through the Nuclear Science User Facilities (NSUF). ** K. acknowledges the support of the NASA Idaho Space Grant Consortium (ISGC) fellowship. Work by S. P. was supported by No. ** Louis Stokes Alliance for Minority Participation (LSAMP) REU program.

Data Availability Statement

The data that support the findings of this study are available from the corresponding author upon reasonable request.

Keywords

Ion irradiation effect, irradiation induced amorphous-to-crystalline transformation, nanotubes, morphological change, disorder-order

Figure Captions

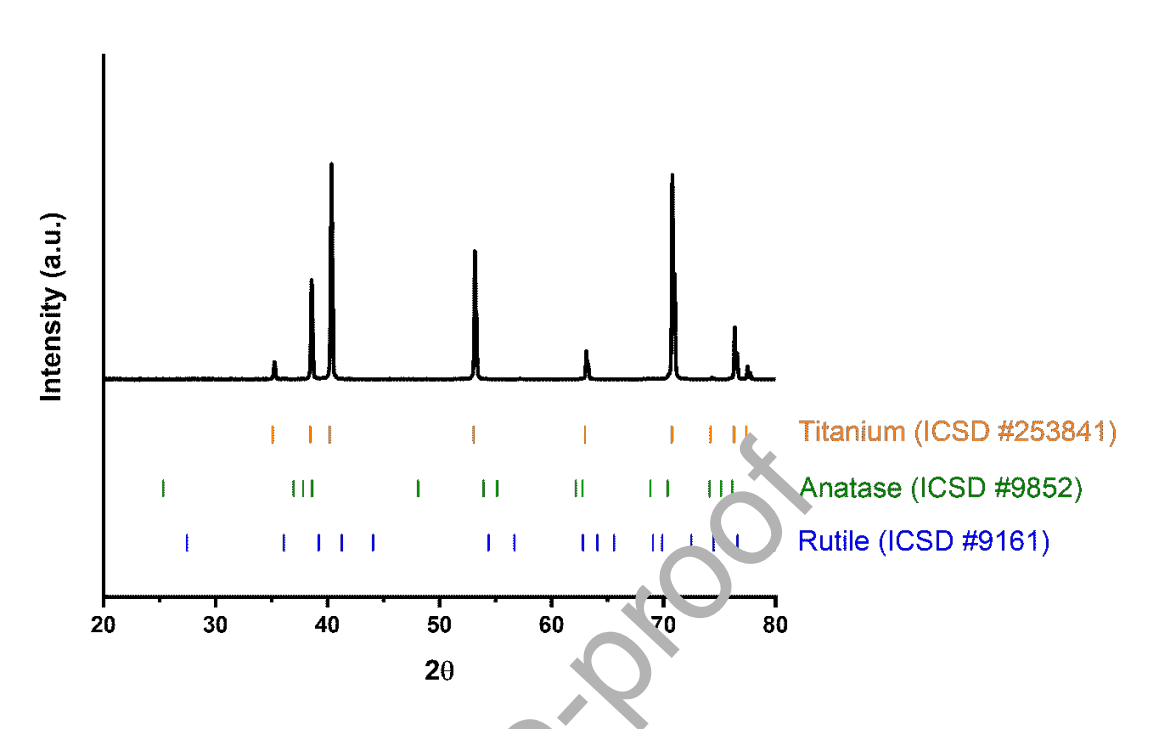


Figure 1. XRD of as-prepared TiO_2 nanotube films price to irradiation experiments.

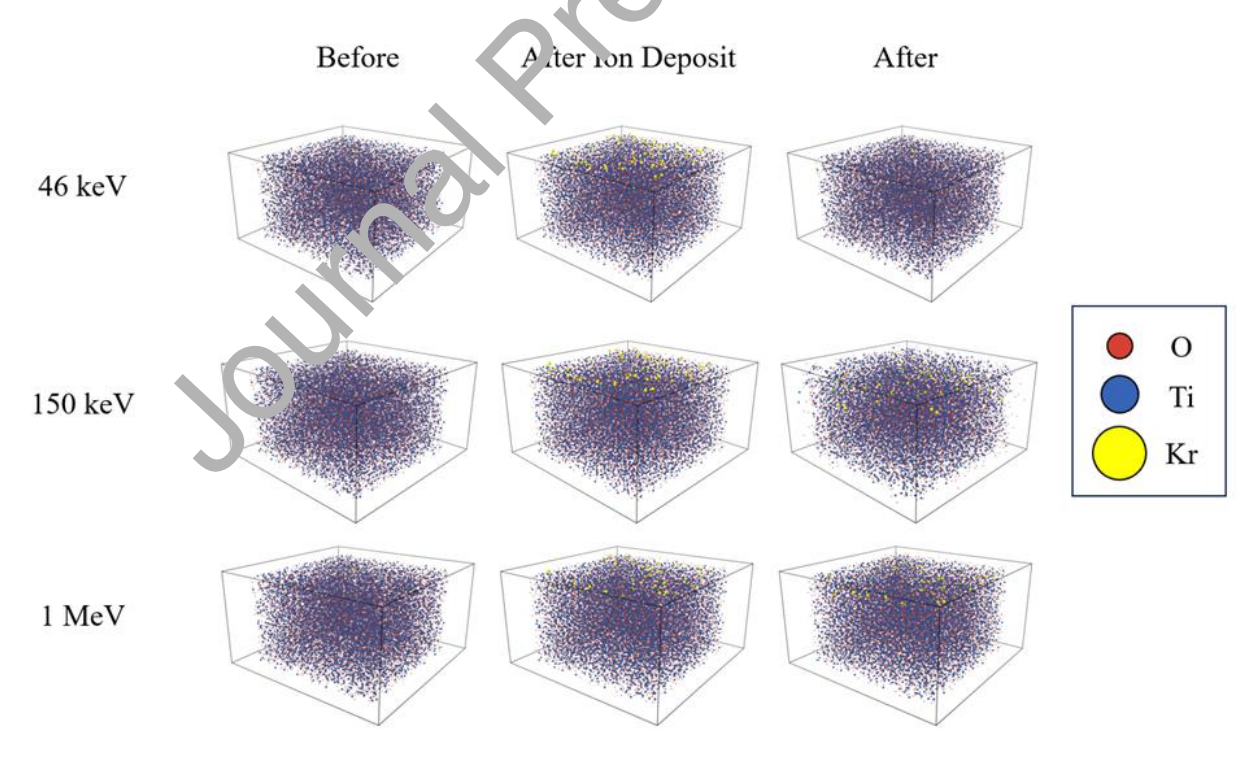


Figure 2. Cell configurations for MD simulation of amorphous TiO₂ before Kr ions are deposited, after Kr ions are deposited, and after diffusion of the Kr ions through the material at various energies.

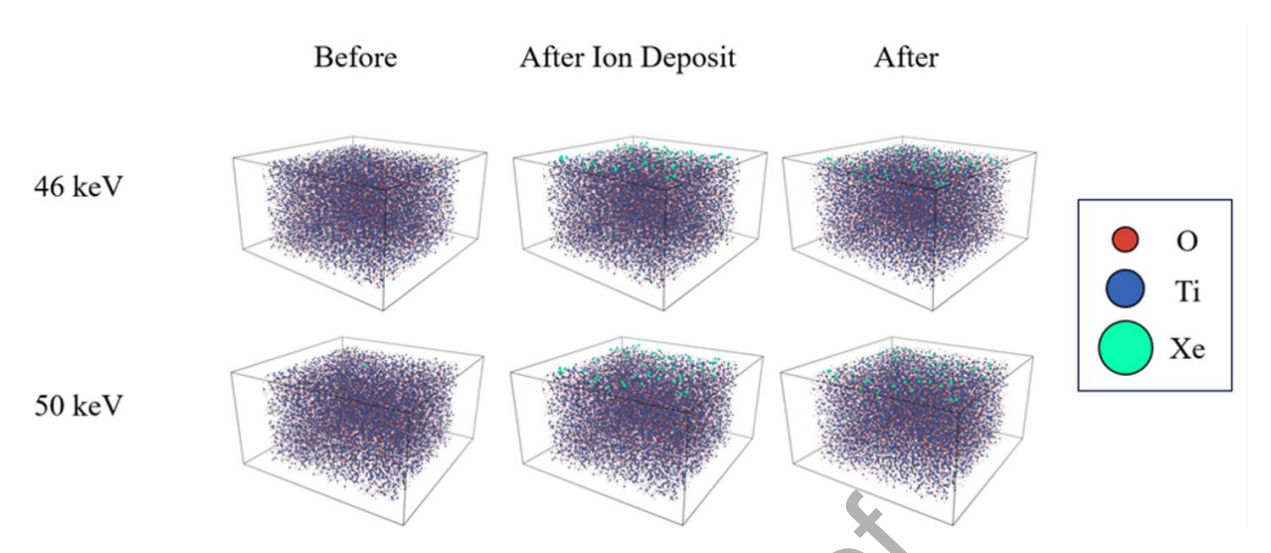


Figure 3. Cell configurations for MD simulation of amorphous TiO_2 before Xe ions are deposited, after Xe ions are deposited, and after diffusion of the Xe ions through the material at various energies.

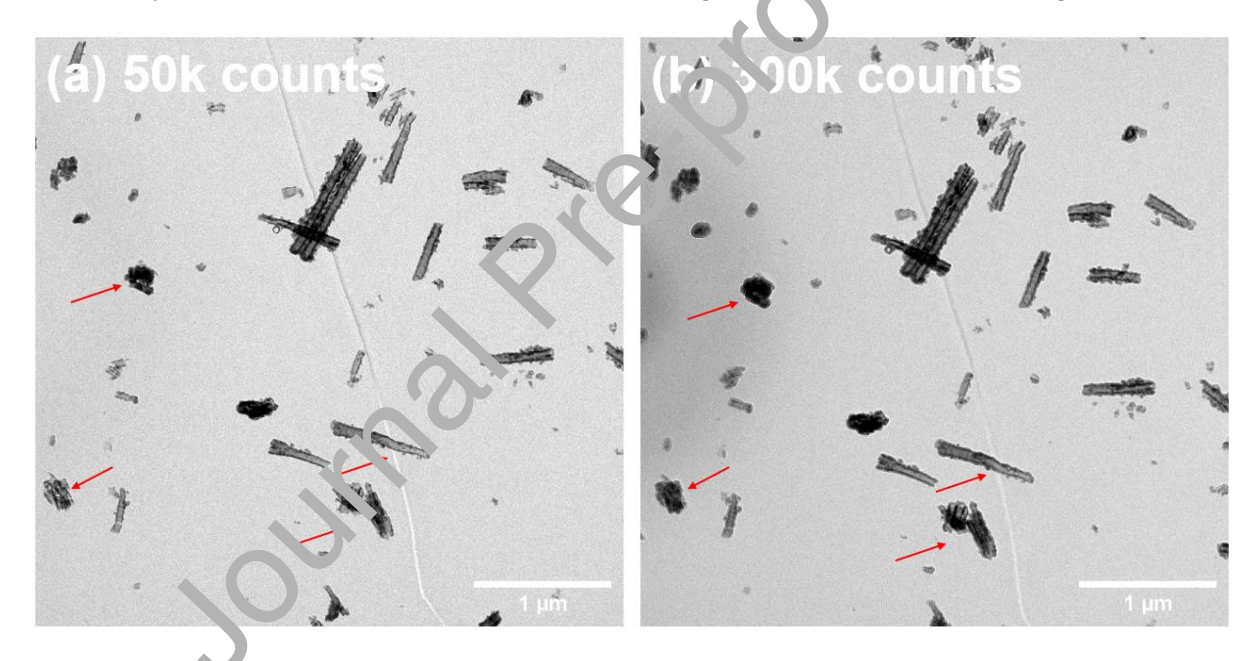


Figure 4. Low magnification TEM images of 46 keV Kr⁺ irradiated nanotubes at (a) 50k ion counts, and (b) 300k counts.

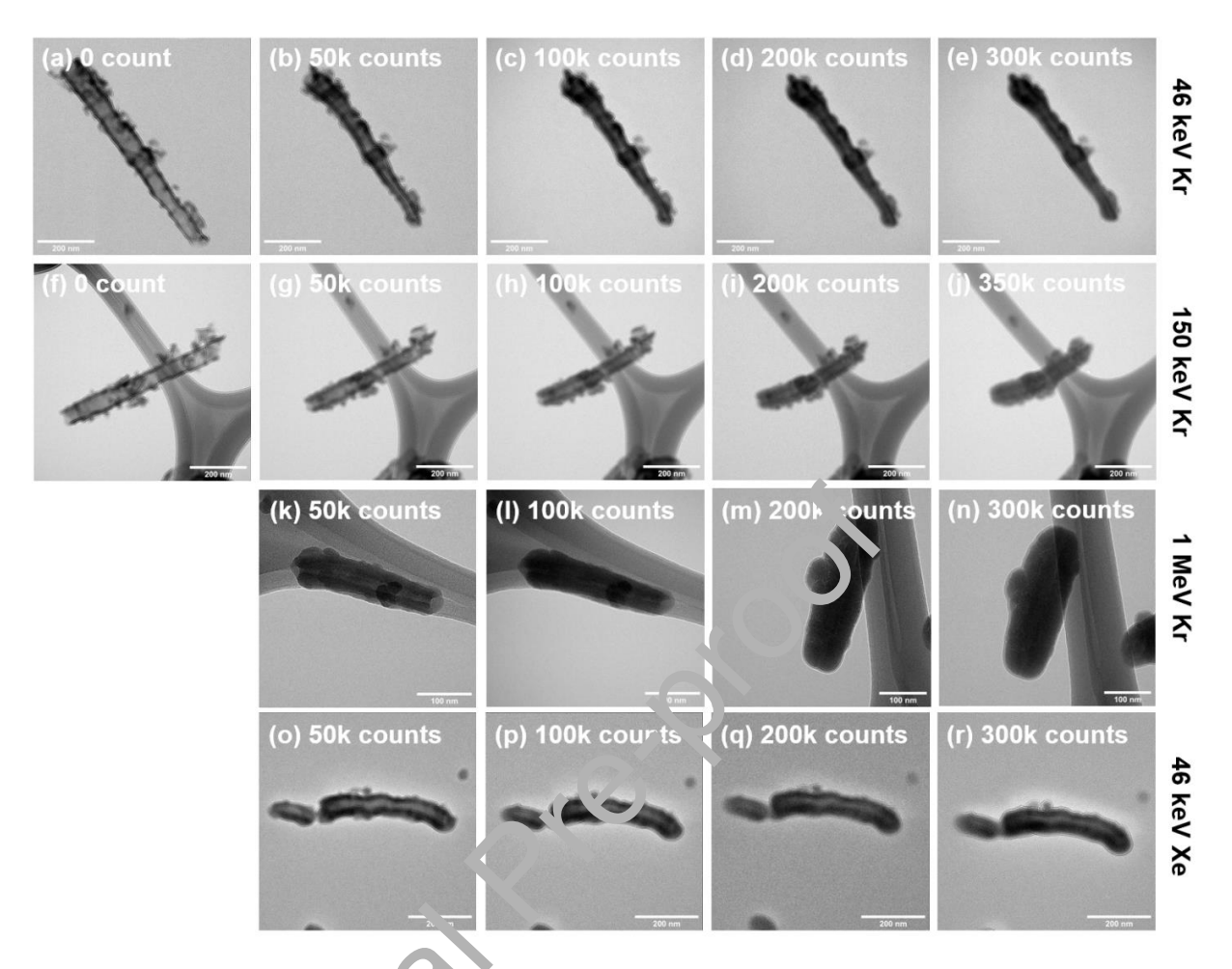


Figure 5. TEM bright field images of *in citu* irradiation evolution of a representative side-view oriented TiO_2 nanotube at intervals of J, 5 k, 100k, 200k, and 300k or 350k counts during (a-e) 46 keV Kr⁺ irradiation, (f-j) 150 keV Kr⁺ irradiation, (k-n) 1 MeV Kr⁺⁺ irradiation, and (o-r) 46 keV Xe⁺ irradiation. Images k-l and m-n are α . Fer ont tube specimens, and no images were taken of the tubes before irradiation.

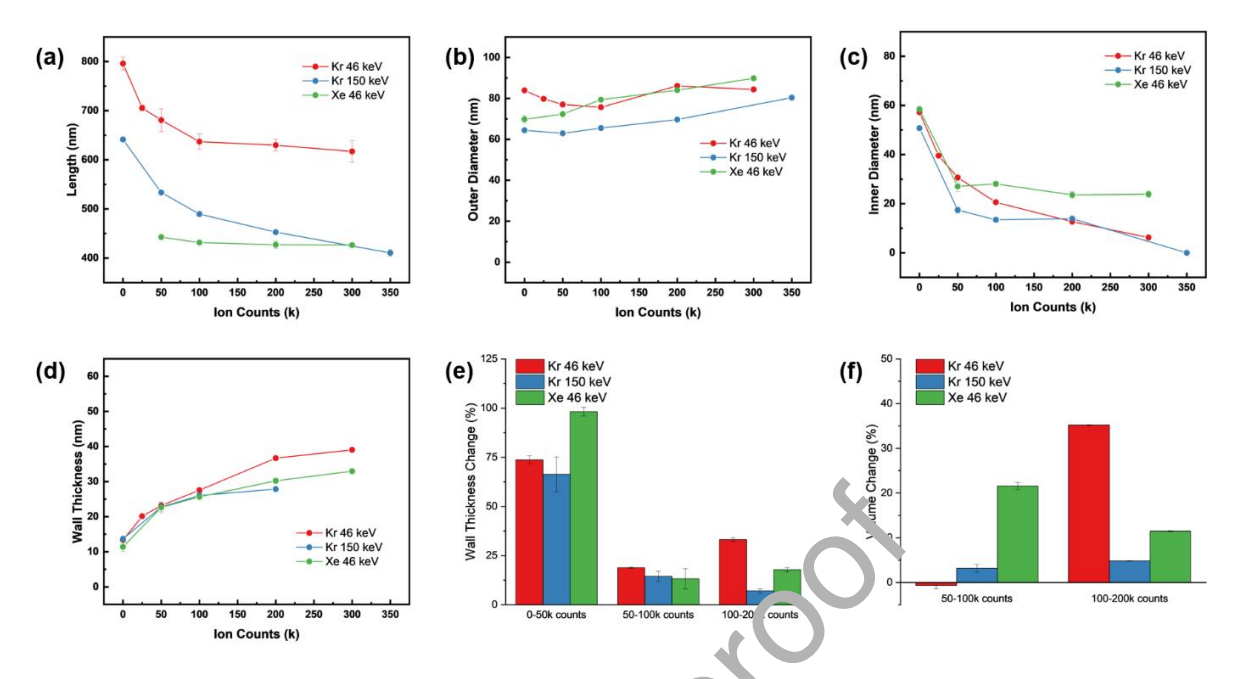


Figure 6. Summary of measurements of nanotube dimensional evolution as a function of ion counts made from TEM images of a side-view TiO_2 nanotube irradiated with 46 keV Kr⁺, 150 keV Kr⁺, and 46 keV Xe⁺: (a) length, (b) outer diameter, (c) inner diameter, and (d) wall thickness. Since an image of the specific Xe⁺ irradiated nanotube before irradiation in not available, values for Xe at a 0 ion count for (b-c) are average values from other unirradiated nanotubes. Percent change of (e) wall thickness in TiO_2 nanotubes at various conditions, and (f) percent volume change at various conditions.

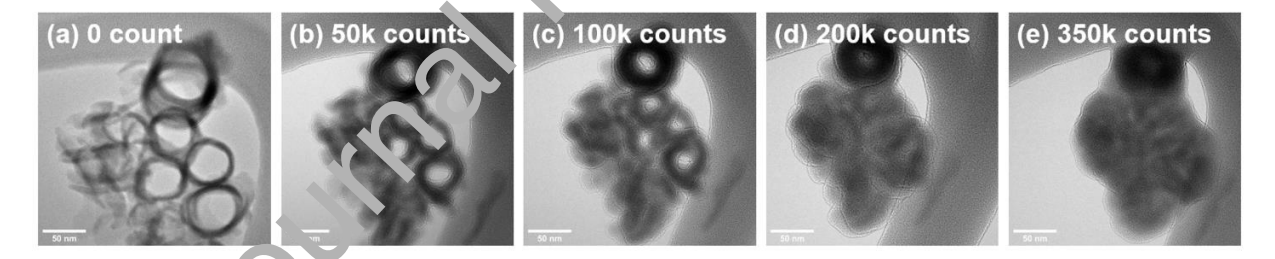


Figure 7. TEM . Tages f om *in situ* irradiation with 150 keV Kr⁺ ions of TiO₂ nanotube fragments irradiated (a-e) parallel to tune long axis.

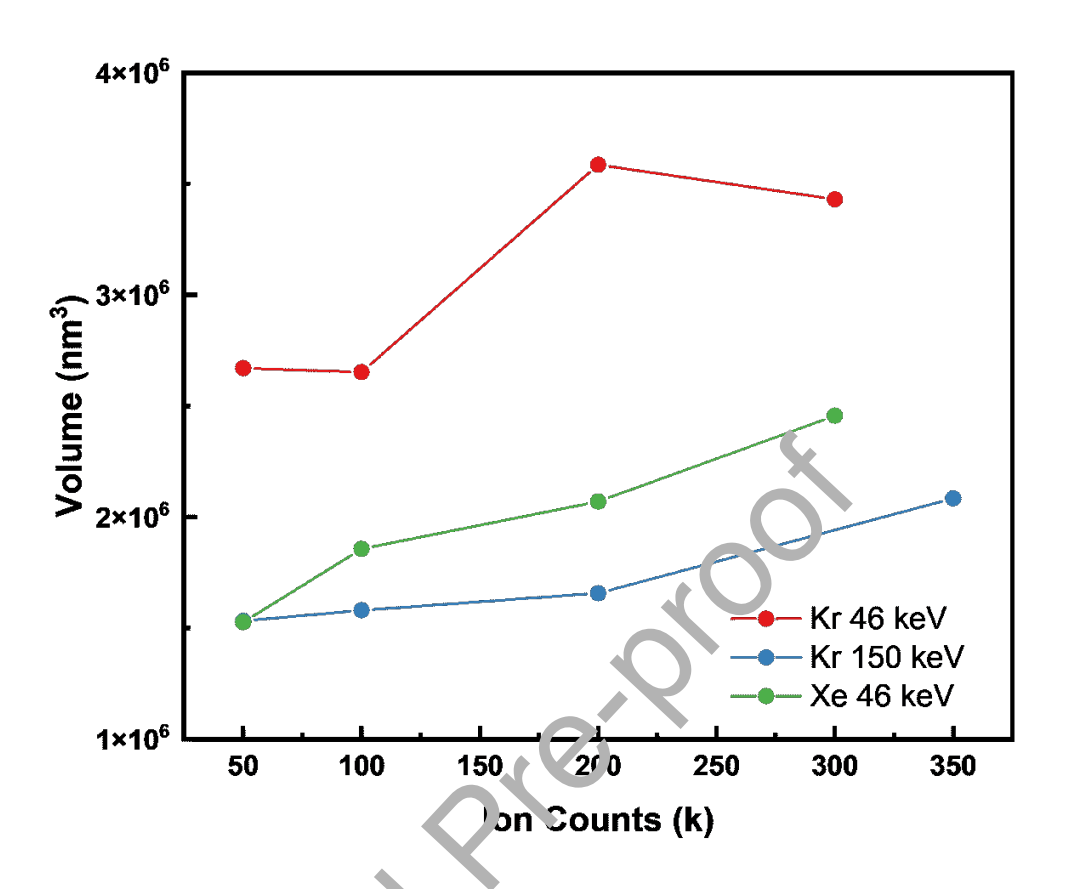


Figure 8. Estimated volume of TiC_2 p includes as a function of ion counts.

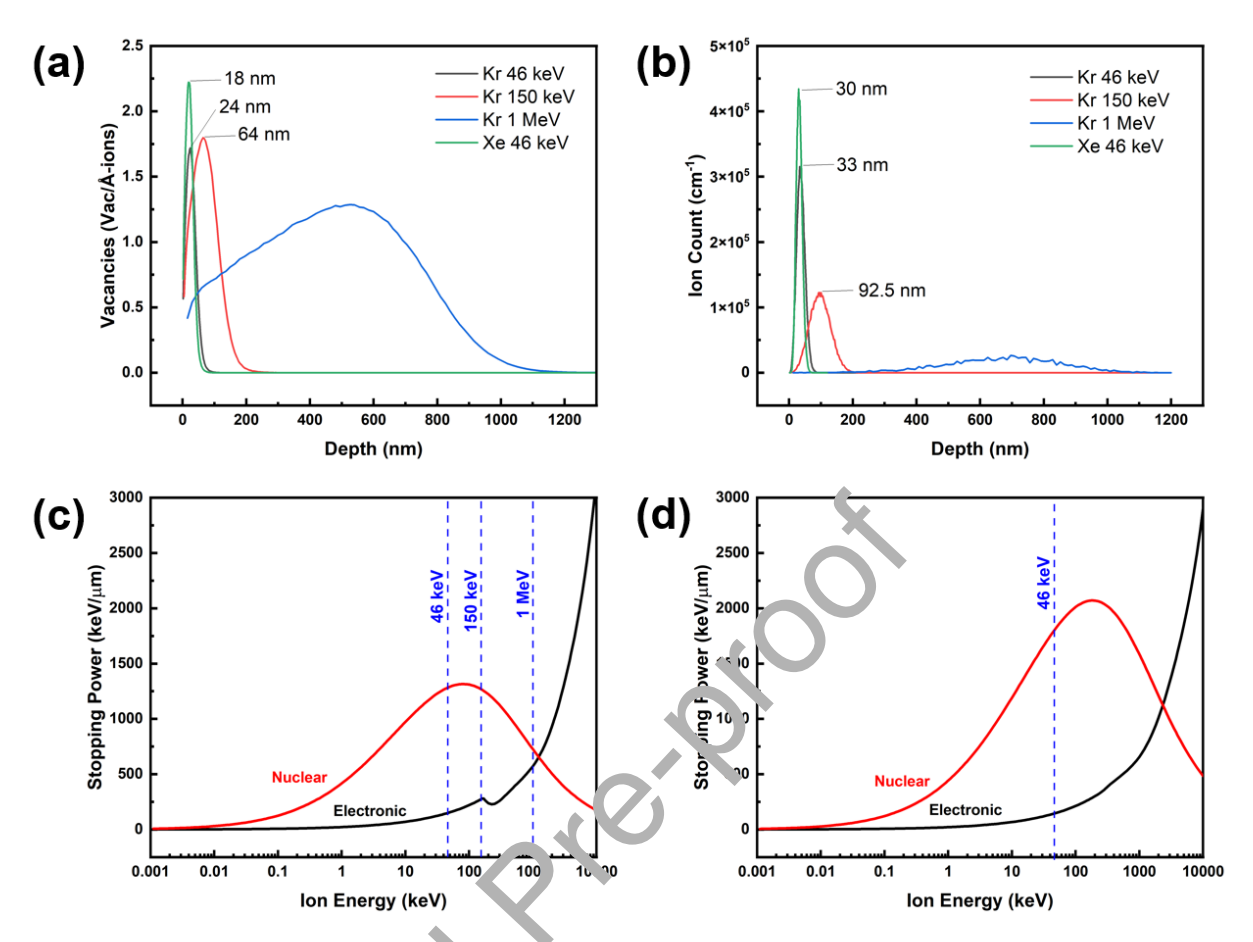


Figure 9. SRIM calculated (a) vacancy concentrations and (b) ion ranges as a function of specimen depth for Kr ion energies of 46 keV, 150 (e^{t}) , 1 NieV, and 46 keV Xe in TiO₂. Electronic and nuclear stopping power for (c) Kr⁺ ions and (d) Ye⁺ io. (e^{t}) in amorphous TiO₂ as a function of ion energy; dashed vertical lines indicate ion energies (e^{t}) in the present study.

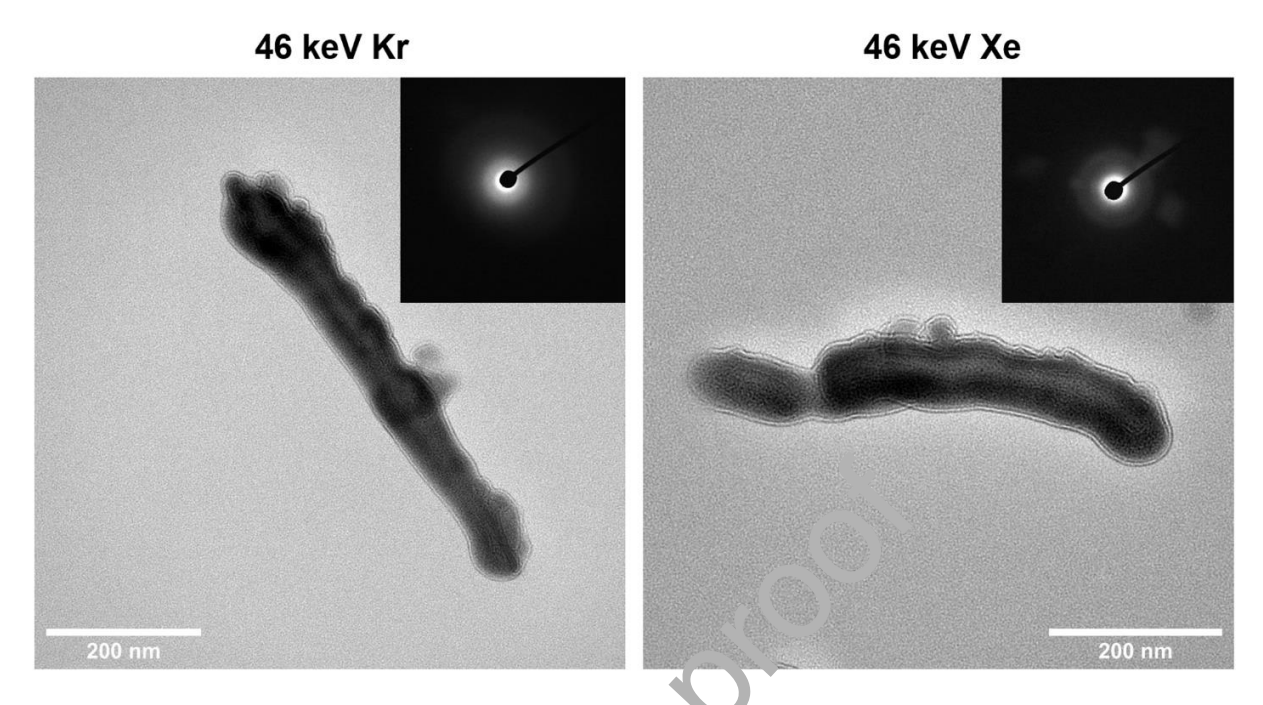


Figure 10. TEM images from separate amorphous TiO_2 NTs. Ger irradiation with 46 keV Kr⁺ and Xe⁺ ions to a count of 300k. Inset image shows SAED patter a equired from the nanotube just after ion irradiation.

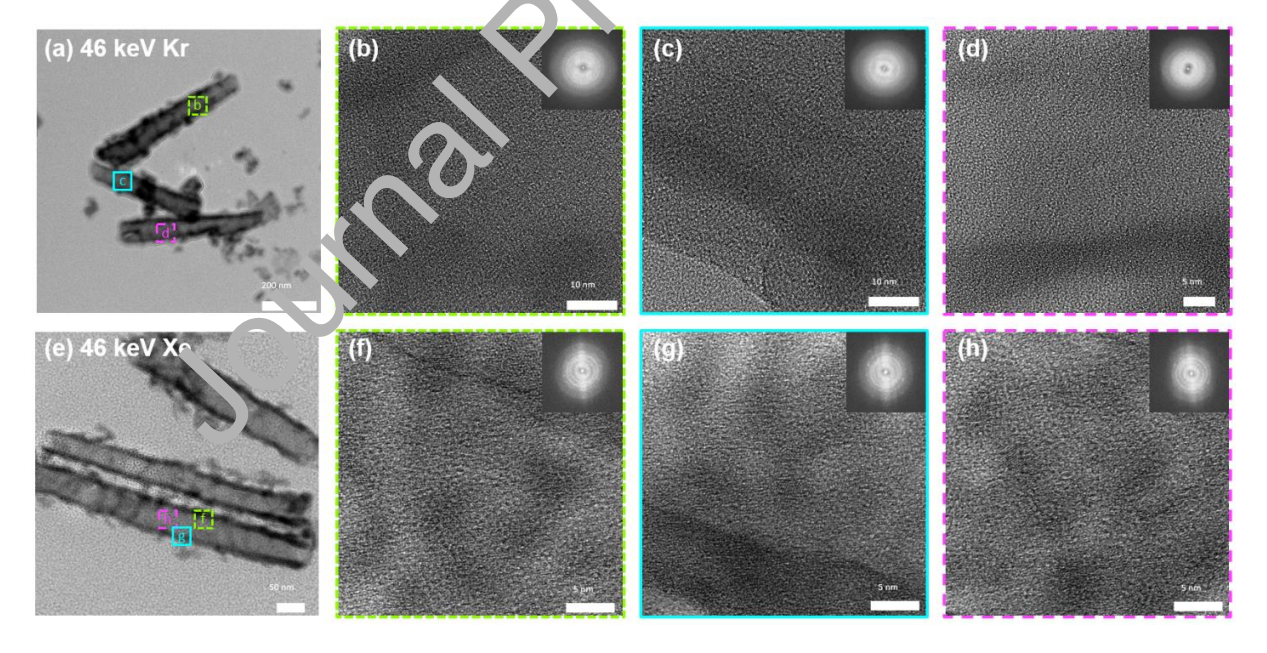


Figure 11. HRTEM images with inset FFT patterns showing (a-d) amorphous nature of nanotubes following 46 keV Kr⁺ irradiation, and (e-h) showing nanocrystallites in amorphous nanotubes following 46 keV Xe⁺ irradiation up to an ion count of 300k.

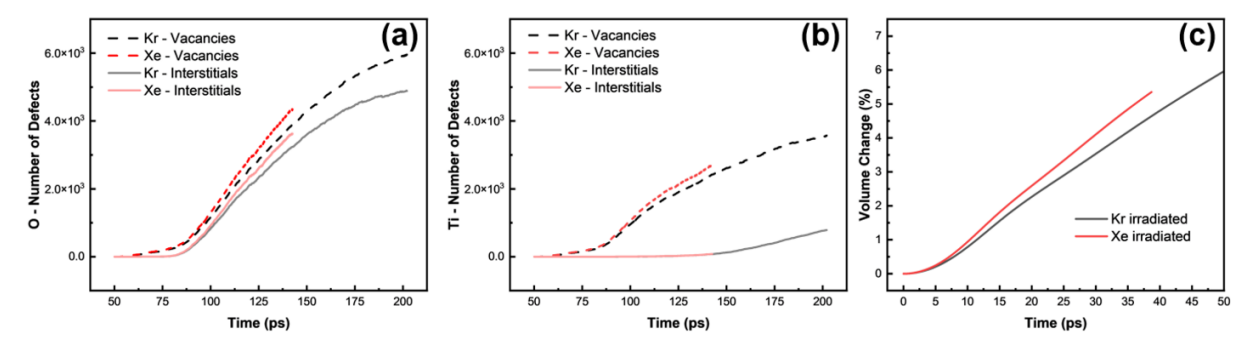


Figure 12. Molecular dynamics simulated time-dependent number of (a) oxygen and (b) titanium vacancies and interstitials, and (c) fractional volume change in amorphous TiO_2 simulation volume, all following 50 keV Kr^+ or Xe^+ irradiation.

References

- (1) Racovita, A. D. Titanium Dioxide: Structure, Impart, and Toxicity. *IJERPH* **2022**, *19* (9), 5681. https://doi.org/10.3390/ijerph19095681.
- (2) Diebold, U. The Surface Science of Titanium D. exice. Surface Science Reports **2003**, 48 (5–8), 53–229. https://doi.org/10.1016/S0167_5725_02)00100-0.
- (3) Carp, O. Photoinduced Reactivity of Tita ii Dioxide. *Progress in Solid State Chemistry* **2004**, *32* (1–2), 33–177. https://doi.org/10.1016/j.progsolidstchem.2004.08.001.
- (4) Fujishima, A.; Honda, K. Electr che nica! Photolysis of Water at a Semiconductor Electrode. *Nature* **1972**, *238* (535), 37–38. https://doi.org/10.1038/238037a0.
- (5) Weinberger, B. R.; Garber, k. B. Titanium Dioxide Photocatalysts Produced by Reactive Magnetron Sputtering. *April. Phys. Lett.* **1995**, *66* (18), 2409–2411. https://doi.org/10.1063/1.1139.x6.
- (6) Wei, M.; Konishi, Y.; Zho, H.; Yanagida, M.; Sugihara, H.; Arakawa, H. Highly Efficient Dye-Sensitized So.' r C. 'ls Composed of Mesoporous Titanium Dioxide. *J. Mater. Chem.* **2006**, *16* (13), 12c7. https://doi.org/10.1039/b514647j.
- (7) Lyczko, M.; Wh. derek, B.; Bilewicz, A. Separation of Radionuclides from Spent Decontamination Fluids via Adsorption onto Titanium Dioxide Nanotubes after Photocatalytic Degradation. *Nanomaterials* **2020**, *10* (8), 1553. https://doi.org/10.3390/nano10081553.
- (8) Chikhray, Y.; Shestakov, V.; Maksimkin, O.; Turubarova, L.; Osipov, I.; Kulsartov, T.; Kuykabayeba, A.; Tazhibayeva, I.; Kawamura, H.; Tsuchiya, K. Study of Li2TiO3+5mol% TiO2 Lithium Ceramics after Long-Term Neutron Irradiation. *Journal of Nuclear Materials* **2009**, *386*–*388*, 286–289. https://doi.org/10.1016/j.jnucmat.2008.12.111.
- (9) Beyerlein, I. J.; Caro, A.; Demkowicz, M. J.; Mara, N. A.; Misra, A.; Uberuaga, B. P. Radiation Damage Tolerant Nanomaterials. *Materials Today* **2013**, *16* (11), 443–449. https://doi.org/10.1016/j.mattod.2013.10.019.
- (10) Koroni, C.; Olsen, T.; Wharry, J. P.; Xiong, H. Irradiation-Induced Amorphous-to-Crystalline Phase Transformations in Ceramic Materials. *Materials* **2022**, *15* (17), 5924. https://doi.org/10.3390/ma15175924.

- (11) Smith, K. A.; Savva, A. I.; Mao, K. S.; Wang, Y.; Tenne, D. A.; Chen, D.; Liu, Y.; Barnes, P.; Deng, C.; Butt, D. P.; Wharry, J. P.; Xiong, H. Effect of Proton Irradiation on Anatase TiO2 Nanotube Anodes for Lithium-Ion Batteries. *Journal of Materials Science* **2019**, *54* (20), 13221–13235. https://doi.org/10.1007/s10853-019-03825-w.
- (12) Smith, K. A.; Savva, A. I.; Deng, C.; Wharry, J. P.; Hwang, S.; Su, D.; Wang, Y.; Gong, J.; Xu, T.; Butt, D. P.; Xiong, H. Effects of Proton Irradiation on Structural and Electrochemical Charge Storage Properties of TiO2 Nanotube Electrodes for Lithium-Ion Batteries. *Journal of Materials Chemistry A* **2017**, *5* (23), 11815–11824. https://doi.org/10.1039/C7TA01026E.
- (13) Smith, K. A.; Savva, A. I.; Wu, Y.; Tenne, D. A.; Butt, D. P.; Xiong, H.; Wharry, J. P. Effects of Intermediate Energy Heavy-ion Irradiation on the Microstructure of Rutile TiO ₂ Single Crystal. *Journal of the American Ceramic Society* **2018**, *101* (9), 4357–4366. https://doi.org/10.1111/jace.15576.
- (14) Yang, C.; Olsen, T.; Lau, M. L.; Smith, K. A.; Hattar, K.; Sel, A.; Wu, Y.; Hou, D.; Narayanan, B.; Long, M.; Wharry, J. P.; Xiong, H. In Situ Jon a radiation of Amorphous TiO2 Nanotubes. *Journal of Materials Research* **2022**, *37* (6), 1144–1155. https://doi.org/10.1557/s43578-022-00516-2.
- (15) Was, G. S. Fundamentals of Radiation Materials Science: Metals and Alloys, Second edition.; Springer: New York, 2017.
- (16) Rasband, W. S. ImageJ, 1997.
- (17) Ziegler, J. F.; Ziegler, M. D.; Biersack, J. P. SPIM The Stopping and Range of Ions in Matter (2010). Nuclear Instruments and Ae hods in Physics Research Section B: Beam Interactions with Materials and Atoms 20.0 268 (11–12), 1818–1823. https://doi.org/10.1016/j.nimb.2010. 22.091.
- (18) Thompson, A. P.; Aktulga, H. M., Lerger, R.; Bolintineanu, D. S.; Brown, W. M.; Crozier, P. S.; In 'T Veld, P. J.; Kohlneyer, A.; Moore, S. G.; Nguyen, T. D.; Shan, R.; Stevens, M. J.; Tranchida, J.; Trott, C.; Plin. pton, S. J. LAMMPS a Flexible Simulation Tool for Particle-Based Materials Lea ling at the Atomic, Meso, and Continuum Scales. *Computer Physics Communications* 2022, 271, 108171. https://doi.org/10.1016/j.cpc.2021.108171.
- (19) Van Duin, A. C. T.: Da. gupta, S.; Lorant, F.; Goddard, W. A. ReaxFF: A Reactive Force Field for Hydroc. rbc rs. *J. Phys. Chem. A* **2001**, *105* (41), 9396–9409. https://doi.org/10.1021/jp004368u.
- (20) Ziegler, J. F.; E'ersack, J. P. The Stopping and Range of Ions in Matter. In *Treatise on Heavy-Ic & Scie Ice*; Bromley, D. A., Ed.; Springer US: Boston, MA, 1985; pp 93–129. https://doi.org/10.1007/978-1-4615-8103-1 3.
- (21) Wigner, E.; Seitz, F. On the Constitution of Metallic Sodium. *Phys. Rev.* **1933**, *43* (10), 804–810. https://doi.org/10.1103/PhysRev.43.804.
- (22) Motta, A.; Tonks, M. *In-Situ Ion Irradiation to Add Irradiation Assisted Grain Growth to the Marmot Tool*; DOE-PSU-8688, 1837940; 2021; p DOE-PSU-8688, 1837940. https://doi.org/10.2172/1837940.
- (23) Uberuaga, B. P.; Bai, X.-M. Defects in Rutile and Anatase Polymorphs of TiO₂: Kinetics and Thermodynamics Near Grain Boundaries. *J. Phys.: Condens. Matter* **2011**, *23* (43), 435004. https://doi.org/10.1088/0953-8984/23/43/435004.
- (24) Ranade, M. R.; Navrotsky, A.; Zhang, H. Z.; Banfield, J. F.; Elder, S. H.; Zaban, A.; Borse, P. H.; Kulkarni, S. K.; Doran, G. S.; Whitfield, H. J. Energetics of Nanocrystalline TiO₂.

- *Proc. Natl. Acad. Sci. U.S.A.* **2002**, *99* (suppl_2), 6476–6481. https://doi.org/10.1073/pnas.251534898.
- (25) Swenson, M. J.; Wharry, J. P. Rate Theory Model of Irradiation-Induced Solute Clustering in b.c.c. Fe-Based Alloys. *JOM* **2020**, *72* (11), 4017–4027. https://doi.org/10.1007/s11837-020-04365-4.
- (26) Meldrum, A.; Boatner, L. A.; Ewing, R. C. Electron-Irradiation-Induced Nucleation and Growth in Amorphous LaPO 4, ScPO 4, and Zircon. *Journal of Materials Research* **1997**, 12 (7), 1816–1827. https://doi.org/10.1557/JMR.1997.0250.
- (27) Qin, W.; Nagase, T.; Umakoshi, Y. Electron Irradiation-Induced Nanocrystallization of Amorphous Fe85B15 Alloy: Evidence for Athermal Nature. *Acta Materialia* **2009**, *57* (4), 1300–1307. https://doi.org/10.1016/j.actamat.2008.11.009.
- (28) Wharry, J. P.; Xiong, H. (Claire); Olsen, T.; Yang, C. Radiation Effects in Battery Materials. In *Encyclopedia of Energy Storage*; Elsevier, 2022; pp 243–255. https://doi.org/10.1016/B978-0-12-819723-3.00109-8.
- (29) Liu, B. X.; Lai, W. S.; Zhang, Q. Irradiation Induced Amorphiz, tion in Metallic Multilayers and Calculation of Glass-Forming Ability from Atomistic Potential in the Binary Metal Systems. *Materials Science and Engineering: R: Reports* 2000, 29 (1–2), 1–48. https://doi.org/10.1016/S0927-796X(00)00016-4.
- (30) Qin, W.; Szpunar, J. A.; Umakoshi, Y. Electron or Jo. Irradiation-Induced Phase-Change Mechanism between Amorphous and Crystallin. State. *Acta Materialia* **2011**, *59* (5), 2221–2228. https://doi.org/10.1016/j.actamat.2010.12.025.
- (31) Dey, S.; Chakravorty, A.; Mishra, S. B.; J. Inc. un, N.; Hazra, A.; Nanda, B. R. K.; Sudakar, C.; Kabiraj, D.; Roy, S. C. Localized The Property Spike Driven Morphology and Electronic Structure Transformation in Swif. H. av, Ion Irradiated TiO 2 Nanorods. *Nanoscale Adv.* **2022**, 4 (1), 241–249. https://doi.org/10.1039/D1NA00666E.
- (32) Schulson, E. M. The Orderic 9 and L isordering of Solid Solutions under Irradiation. *Journal of Nuclear Materials* **1979** *§*3 (2), 239–264. https://doi.org/10.1016/0022-3115(79)90610-X
- (33) Mayr, S. G. The Role of You Aradiation Induced Viscous Flow in Thin Film Structuring: Hard Matter Going Sof In *Advances in Solid State Physics*; Kramer, B., Ed.; Advances in Solid State Physics; Springer-Verlag: Berlin/Heidelberg, 2005; Vol. 45, pp 327–338. https://doi.org/10.1007/11423256026.
- (34) Xu, X.; He'nig, K.-H.; Möller, W.; Engelmann, H.-J.; Klingner, N.; Gharbi, A.; Tiron, R.; Borany, J. V. Hawacek, G. Morphology Modification of Si Nanopillars under Ion Irradiation at Elevated Temperatures: Plastic Deformation and Controlled Thinning to 10 Nm. Semicond. Sci. Technol. 2020, 35 (1), 015021. https://doi.org/10.1088/1361-6641/ab57ba.
- (35) Yang, W.; Pang, J.; Zheng, S.; Wang, J.; Zhang, X.; Ma, X. Interface Effects on He Ion Irradiation in Nanostructured Materials. *Materials* **2019**, *12* (16), 2639. https://doi.org/10.3390/ma12162639.
- (36) Camara, O.; Mir, A. H.; Dzieciol, K.; Greaves, G.; Basak, S.; Kungl, H.; Bosi, M.; Seravalli, L.; Donnelly, S. E.; Eichel, R. A.; Hinks, J. A. Nanostructuring Germanium Nanowires by In Situ TEM Ion Irradiation. *Part & Part Syst Charact* **2021**, *38* (12), 2100154. https://doi.org/10.1002/ppsc.202100154.
- (37) CAWTHORNE, C.; FULTON, E. J. Voids in Irradiated Stainless Steel. *Nature* **1967**, *216* (5115), 575–576. https://doi.org/10.1038/216575a0.

- (38) Shewmon, P. G. Radiation-Induced Swelling of Stainless Steel. *Science* **1971**, *173* (4001). https://doi.org/10.1126/science.173.4001.987.
- (39) Mao, K. S.; French, A. J.; Liu, X.; Wu, Y.; Giannuzzi, L. A.; Sun, C.; Dubey, M.; Freyer, P. D.; Tatman, J. K.; Garner, F. A.; Shao, L.; Wharry, J. P. Microstructure and Microchemistry of Laser Welds of Irradiated Austenitic Steels. *Materials & Design* **2021**, *206*, 109764. https://doi.org/10.1016/j.matdes.2021.109764.
- (40) Getto, E.; Nathan, N.; McMahan, J.; Taller, S.; Baker, B. Understanding Radiation Effects in Friction Stir Welded Ma956 Using Ion Irradiation and a Rate Theory Model. *Journal of Nuclear Materials* **2022**, *561*, 153530. https://doi.org/10.1016/j.jnucmat.2022.153530.

Daal	aration	-t:-	+
ואברו	ISTSTAN	OT IN	TOPOCTO

☑ The authors declare that they have no known competing financial interasts or personal relationships that could have appeared to influence the work reported in this papar.
☐The authors declare the following financial interests/prise natirelationships which may be considered as potential competing interests: